Towards Linking Diffusion MRI based Macro-and Microstructure Measures with Cortico-Cortical Transmission in Brain Tumor Patients

Patryk Filipiak, Fabien Almairac, Théodore Papadopoulo, Denys Fontaine, Lydiane Mondot, Stéphane Chanalet, Rachid Deriche, Maureen Clerc, Demian Wassermann

Towards Linking Diffusion MRI based Macro- and Microstructure Measures with Cortico-Cortical Transmission in Brain Tumor Patients

Patryk Filipiak[a,*], Fabien Almairac[b], Théodore Papadopoulo[a], Denys Fontaine[b], Lydiane Mondot[c], Stéphane Chanalet[c], Rachid Deriche[a], Maureen Clerc[a], Demian Wassermann[a,d]

[a]*INRIA, Université Côte d'Azur, France*
[b]*Service de Neurochirurgie, CHU de Nice, Université Côte d'Azur, France*
[c]*Service de Radiologie, CHU de Nice, Université Côte d'Azur, France*
[d]*INRIA, CEA, Université Paris-Saclay, France*

Abstract

We aimed to link macro- and microstructure measures of brain white matter obtained from diffusion MRI with effective connectivity measures based on a propagation of cortico-cortical evoked potentials induced with intrasurgical direct electrical stimulation. For this, we compared streamline lengths and log-transformed ratios of streamlines computed from presurgical diffusion-weighted images, and the delays and amplitudes of N1 peaks recorded intrasurgically with electrocorticography electrodes in a pilot study of 9 brain tumor patients. Our results showed positive correlation between these two modalities in the vicinity of the stimulation sites (Pearson coefficient 0.54±0.13 for N1 delays, and 0.47±0.23 for N1 amplitudes), which could correspond to the neural propagation via U-fibers. In addition, we reached high sensitivities (0.78±0.07) and very high specificities (0.93±0.03) in a binary variant of our comparison. Finally, we used the structural connectivity measures to predict the effective connectivity using a multiple linear regression model, and showed a significant role of brain microstructure-related indices in this relation.

Keywords: structural connectivity, brain white matter microstrucure, effective connectivity, cortico-cortical evoked potentials, direct electrical stimulation, tractography

1. Introduction

Diffusion Magnetic Resonance Imaging (dMRI) provides measures of brain macro- and microstructure noninvasively, although their accuracy is still undetermined [1, 2, 3, 4]. In particular, dMRI-based tractography is considered insufficient to guide brain tumor resection due to inaccuracies in localizing cortical terminations of fiber bundles [2, 5, 6, 7, 8]. From the clinical perspective, invasive electrophysiological mapping with Direct Electrical Stimulation (DES) [9, 10, 11] remains the "gold standard" for probing connectivity [12, 13] when resecting a tumor located in eloquent brain areas [7, 14], as it allows to optimize the extent of resection [15] and accommodate inter-patient variability [16]. However, a clinical use of DES is mostly based on empirical knowledge and hardly reveals

---

any structural information about neural connections affected by the stimulation [7, 8]. In this paper, we study the link between complementary information about brain connectivity arising from the dMRI- and DES-based approaches.

DES of the brain cortex excites pyramidal cells at the stimulation site and induces an evoked potential that propagates through White Matter (WM) bundles to distal cortical regions [17, 18, 19, 20]. Matsumoto et al. [17] were the first ones to call this behavior a Cortico-Cortical Evoked Potential (CCEP). In the clinical scenario of craniotomy, CCEPs can be monitored with Electrocorticography (ECoG) electrodes, which allow to probe the effective brain connectivity, i.e. "the influence one neural system exerts over another" [21]. Such ability to trigger CCEPs with DES and monitor their propagation with ECoG offers a rare opportunity to acquire ground truth information about neural connections inside a particular brain [17, 18, 19, 20]. Conner et al. [18] used this method to validate tractography, while Silverstein et al. [22] have recently suggested to integrate the propagation of CCEPs with pathlengths and Fractional Anisotropy measures from dMRI to jointly probe the cortico-cortical networks. In this work, we propose to engage both macro- and microstructure information into this joint study of brain connectivity.

From the technical perspective, CCEPs typically consist of four consecutive voltage peaks named P1, N1, P2, and N2 [17, 23, 24], where N are negative peaks while P are positive ones[1] (Figure 1). Nonetheless, hitherto studies of CCEPs mostly concentrate on monitoring N1, which is attributed to excitation of pyramidal cells [19, 27]. Furthermore, N1 is usually more pronounced in the recorded signal than the other peaks [28, 25], which designates it as the most distinctive feature to study. In our work, we measured both delays and amplitudes of N1 in order to probe the propagation of CCEPs along WM tracts.

[Figure 1 about here.]

Our goal was twofold. First, we aimed to validate our dMRI-based structural connectivity measures using the CCEP-based effective connectivity as reference. For this, we correlated the measures of fiber pathways, including aggregated streamline lengths and log-transformed counts of streamlines that connected the stimulation sites and the recording electrodes, with the delays and amplitudes of N1s. Earlier studies [18, 19, 22, 29] showed a linear relation between these quantities, so we fitted a linear regression model to predict the effective connectivity with our macrostructural measures.

As the second goal, we addressed the variability of neural conduction at the microstructure level, which depends on axon diamater, myelin sheath thickness, and axonal membrane properties [30]. For this, we incorporated into our regression model a set of microstructure indices that quantify the tissue composition. Whenever possible, we preferred the clinically feasible metrics derived from Diffusion Tensor Imaging [31] (DTI) or Diffusional Kurtosis Imaging [32] (DKI), e.g. axonal water fraction volume or tortuosity of the extra-axonal geometry [33]. For those requiring long multishell acquisition, we used Mean Apparent Propagator with Laplacian regularization [34] (MAPL) signal representation.

---

[1]An alternative naming convention is also used in the literature, according to which the positive peaks are enumerated from zero, wherein P1 is referred to as P0, and P2 as P1 [25, 26].

Our work contributes to the study of the structural underpinnings of the CCEP-based effective connectivity. Despite being used in the clinical practice, little is known about the propagation of DES-induced evoked potentials along WM tracts [25]. Hitherto research in this domain [13, 17, 18, 19, 29, 24, 35], performed on epileptic patients, led to discoveries in neuronal conduction [17, 29, 35] and pathological zone characterization [13]. However, a generalization of findings from patients with a single type of pathology to normal brain networks raised reasonable criticism [19]. Yamao et al. [20] addressed this issue by repeating the same experiment on brain tumor patients, reaching similar results. Here, we adapted their methodology to common clinical conditions of a brain tumor surgery, which implied a use of low-current DES (2-5 mA instead of 10-15 mA) and small-sized stimulating electrodes (5 mm between poles rather than 10 mm). Thanks to these modifications, an integrated study of effective and structural brain connectivity, suggested by Silverstein et al. [22], would become available in a broader set of patients. More importantly, though, our endeavour to predict CCEPs with dMRI-based data aimed to explain the role of brain macro- and microstructure in the cortico-cortical transmission. Having this, we could apply our structural model to anticipate the clinically valuable effective connectivity measures prior to craniotomy or use this information when treating patients that need no surgical intervention.

We report here our pilot study of 9 patients. For each of them, we correlated presurgical dMRI-based structural connectivity measures, including streamline counts and lengths, with delays and amplitudes of N1. In addition, we considered binary variants of the above quantities to assess the structural connectivity thresholds for CCEPs. Finally, we used the macro- and microstructure measures of WM to predict the CCEP propagation using a multiple linear regression model. Our results show a significant role of microstructure indices in this relation.

2. Methods

This study, approved by the French national ethics committee and registered in the Clinical Trials database (NCT 03503110) [36], did not modify the usual surgical nor brain mapping protocols.

Our data set consisted of newly acquired anonymized presurgical dMRI and intrasurgical ECoG signal recordings, both of which we describe in detail later in this section. They are not publicly available due to restrictions imposed by the administering institution. The authors will share them by request from any qualified investigator after completion of a data sharing agreement.

The source code for the data post-processing, correlation study, and prediction of CCEPs is available for download at: `https://doi.org/10.5281/zenodo.3989987` [37].

2.1. Patients

We considered 9 patients (5 female) aged 23-66 (40±13) undergoing brain tumor resection (Table 1) under wide-awake local anesthesia. The selection criteria included lesions located inside or near the perisylvian area, which is a relatively well-studied brain region regarding CCEP-based effective connectivity [17, 18, 19, 20, 24].

Each patient signed an informed written consent to participate in our study. All of them received the same antiepileptic medication (Levetiracetam). Only Patient 6 had a history of previous anticancer treatment (Table 1).

[Table 1 about here.]

2.2. Surgical settings

All patients in this study were operated in the Asleep-Awake-Asleep protocol [38]. This created an opportunity for us to observe clinical responses to DES applied in the awake condition and to record brain electrophysiological activity resulting from DES under general anesthesia.

2.3. Data acquisition

Diffusion MRI. We acquired presurgical diffusion MR images with 2x2x2 mm voxel size resolution. Our protocol comprised 4 shells having $b \in \{400, 800, 1550, 3100\}$ [s/mm^2] with $\{6, 13, 29, 51\}$ directions, respectively, interleaved with 6 images without diffusion weighting ($b = 0$). The pulse width was $\delta = 0.0322$ s and the diffusion time $\Delta = 0.0450$ s. We used the above acquisition parameters since they maximized image reconstruction accuracy of the MAPL signal representation [34] under the constraint of 25 minutes of imaging time on the clinical GE 3T-scanner. The MAPL helped us obtain numerous brain microstructure indices [39] that we present in Subsection 2.6.

Direct electrical stimulation. A spatial distance between anode and cathode of a stimulation probe, and a current intensity of DES are two crucial parameters that determine a volume of brain tissue that is excited in our experiment [28]. However, neither of them can be freely altered. The former parameter is fixed by the probe manufacturer. In our study, we used common-type probes with 5-millimeter separation between poles. The latter parameter, current intensity, must be adapted to each patient individually by the neurosurgeon [8], leaving very little room for modifications. In our experiment, the current intensities lied in the range of 2-5 mA (Table 2).

Other DES parameters offer more flexibility. In particular, the clinically used stimulation frequencies are 50-60 Hz [28]. Nonetheless, for the purpose of recording CCEPs, much smaller values must be used since a typical electrical response to DES lasts about 250 ms or more [17, 19, 18]. We started with 5 Hz for Patient 1. Then, we decreased the frequency to 2 Hz for all the remaining patients, aiming to extend the observed time window from 200 to 500 ms (Table 2). In each case, we applied biphasic square wave pulse of the width 2×1 ms.

[Table 2 about here.]

Electrocorticography. We used sterile strips of ECoG subdural electrodes manufactured by DIXI Medical®. The electrodes had 4 mm contact diameter with 10 mm center-to-center distance between electrodes within each strip. Depending on the size of a bone flap in a given patient's skull and the accessible area of the cortex, we placed 2 or 3 strips. Their configuration comprised one or two short strips with 4 electrodes each and/or one longer strip with 6 electrodes, totaling 8, 10, or 14 recording electrodes (Table 2). For every patient, we positioned the strips in alignment

4

with the cortical terminations of Arcuate Fasciculus (AF) and Superior Longitudinal Fasciculus III (SLF3) obtained from tractography (Figure 2a).

[Figure 2 about here.]

We recorded the ECoG signal right after tumor resection, while the patient was under general anesthesia. During the acquisition, the neurosurgeon stimulated consecutive cortical sites located in the proximity of all accessible electrodes. Note that parts of strips could be inserted beyond the bone flap, slipped between the dura matter and the cortex, allowing to record the signal in areas inaccessible to stimulation (Figure 2b). We used a 32-channel signal amplifier manufactured by TMSi® with our recording electrodes set to the common reference mode, the ground electrode placed on the patient's back, and all the remaining inputs being short-circuited. Finally, the recordings were made using ASALAB software by ANT Neuro® with a 2 kHz sampling rate.

2.4. Structural connectivity

For each patient, we ran probabilistic tractography algorithm iFOD2 [40] twice, using the same dMRI data acquired prior to the surgery. The first run was destined for surgical planning and neuronavigation. To this end, we computed a whole-brain tractogram containing one million streamlines. From that, we dissected AF and SLF3, as mentioned earlier, using MI-Brain software by Imeka®. Next, we overlaid the streamlines of interest on a T1-weighted image that we transferred into the neuronavigation system produced by Brainlab®. In the operating room, the neurosurgeon placed the ECoG electrodes on the cortex in the precise locations of the WM bundle terminations indicated with tractography and localized spatially with the neuronavigation system (Figure 2).

Our second tractography was performed retrospectively, after a surgery. Here, we considered two types of Regions Of Interest (ROIs): *seeding ROIs* centered in the stimulation sites and *target ROIs* centered in the ECoG electrode locations. We obtained their spatial coordinates from the neuronavigation system that had been used during the surgery. Note that these coordinates referred to the points on the cortex, whereas tractography algorithms typically produce streamlines originating at the white/gray matter boundary [2]. We accounted for this by defining our ROIs as spheres with 10-mm diameter, centered at the cortex (Figure 3), which is a common practice in such scenarios [41]. Next, for each seeding ROI, we ran the DIPY implementation [42] of the probabilistic tractography algorithm iFOD2 using 5,000 random seeds per voxel. The step size equaled 0.5mm with the maximum angle of $30°$. We set the maximum streamline length to 500 mm and defined the threshold on Generalized Fractional Anisotropy (GFA < 0.25) as a stopping criterion. From all the streamlines produced, we only retained those that touched any part of the target ROIs. As illustrated in Figure 3, the shortest streamlines thus obtained often originated and terminated near the boundaries of spherical ROIs, which led to underestimation of the streamline lengths. As a compensation, we increased the streamline lengths with the average distances to the centers of ROIs on both ends (2×3.7mm in this study[2]).

---

[2]3.7mm was the average distance between any voxel within our 10mm spherical ROI and the center of this ROI.

[Figure 3 about here.]

Having these, we computed the log probabilities of succeeding the Monte Carlo connectivity experiment. Technically, we divided the streamline counts by the total number of seeded tracts and applied $\log_{10}$ transform to account for the streamlines distribution which is known to be biased toward shorter links [13, 43, 44]. Then, we took reciprocal values of our log-transformed streamline counts ($-log\ count$) to ensure the same monotonicity type as in the length-based macrostructural measures and thus obtained coherent presentation of results.

2.5. Effective connectivity

Our ECoG recordings were multi-channel time series with manually triggered time tags marking stimulation events. In post-processing, we epoched the data and zeroed out stimulation artifacts. Next, we subtracted the common average (i.e. an average of all recording electrodes at a given time) from the signal to reduce the noise induced by short-circuited inputs and remove ECG artifacts. Finally, we averaged the epochs to increase signal to noise ratio.

A typical CCEP consists of four consecutive voltage peaks named P1, N1, P2, and N2 [17, 23, 24], where N are negative peaks while P are positive ones (Figure 1). In this work, we studied the propagation of N1s, which we were able to identify with the highest confidence among the three voltage peaks recorded in our ECoG signals. To this end, we implemented a Python script that recognized characteristic U-shaped patterns of N1s based on the derivative of the signal. In order to reduce noise, we applied a 30Hz low-pass filter prior to identifying N1s. As a result, we were confident about the peaks that we found, although we might have potentially disregarded some of the less reliable ones due to their low amplitudes.

2.6. Correlation between structural and effective connectivity

After post-processing of our dMRI and ECoG data, we sought to evaluate a relation between the tractography-based macrostructural information and the effective connectivity measures. We approached this in two manners. First, by correlating streamline lengths and streamline counts ($-log\ count$) with N1 delays and N1 amplitudes. Second, by comparing binary variables which determined either a presence or an absence of structural and/or effective connection between endpoints. Such a comparison at the binary level helped us assess the structural thresholds above which CCEPs were observed and approximate the rate of false positives among selected tractography results, as we will explain later (in Section 4.2).

In the first approach, we defined the following three distance measures (given in millimeters) to quantify the streamline-based information:

- **minimum streamline length** (*min str*) — a length of the shortest streamline connecting a given pair of endpoints, as in Silverstein et al. [22], plus the correction described in Subsection 2.4;

- **median streamline length** (*med str*) — as above, using median instead of minimum;

6

- **distance along WM surface** (*wm dist*) — a length of the shortest path connecting a given pair of endpoints traced along the surface of WM using Freesurfer [45].

In the second approach, we defined binary effective connectivity by labeling the pairs of endpoints between which we observed a propagation of CCEPs as *effectively connected* and all the remaining ones as *effectively disconnected*.

The case of binary structural connectivity was not so straightforward, since almost all pairs of ROIs in our data sets were joined with dMRI-based streamlines. In accordance with the previous studies, including Maier-Hein et al. [1], Thomas et al. [4], de Reus et al. [46], we assumed that a considerable number of links associated with lowest connectivities were false positives. Hence, we introduced a cut-off threshold on the macrostructural connectivity measures that would filter out potentially spurious links. All the pairs of endpoints for which the respective measure surpassed the threshold would be considered as *structurally connected*, whereas all those below the threshold would be considered as *structurally disconnected*. However, there is no common agreement on which cut-off values are most appropriate in such scenarios. Parker et al. [13] used an arbitrary threshold for the whole study. Here, we adjusted the cut-off values per subject to account for the inter-patient variability and the differences in the DES parameters. To this end, we defined connectivity matrices $M = [m_{ij}]$ representing stimulation sites as rows and recording electrodes as columns. In the length-based connectivity matrices, we computed the coefficients by dividing *min str* distances between $n > 0$ source and $m > 0$ target ROIs by a sum of all such distances as follows

$$\forall_{i=1,...,n} \forall_{j=1,...,m} \quad m_{ij} = \frac{\min \text{str}_{ij}}{\sum_{i=1,...,n} \sum_{j=1,...,m} \min \text{str}_{ij}}. \tag{1}$$

In the count-based one, we used the log-transformed streamline counts instead of *min str*. This way, we obtained two probability distributions, a length-based and a count-based one.

Next, we sought cut-off values ensuring best agreement between the binary structural connectivity maps and the binary effective connectivity maps. Following Parker et al. [13], we used Jaccard Index (JI) for this purpose. Let us recall that JI measures a ratio between an intersection and a union of two sets. When applied to binary maps, it computes their mutual similarity score. Hence, by maximizing JIs, we obtained cut-off values on the count- and length-based probabilities that maximized agreement between the macrostructural and effective connectivity measures.

Finally, we estimated the size of area affected by DES using macrostructural measures. For this, we quantified the streamlines that linked any two (binary) effectively connected regions.

2.7. Prediction of effective connectivity empowered with microstructure indices

Taking into account that propagation of evoked potentials is related to tissue microstructure (e.g. properties of nodes of Ranvier [47] or axon diameter [48, 49]), we extended our set of macrostructural measures obtained from dMRI by quantities related to the brain WM microstructure, namely:

- **DTI metrics** [31] — Fractional Anisotropy (FA); Mean (MD), Axial (AD), and Radial Diffusivity (RD).

7

- **DKI metrics** [32] — Mean (MK), Axial (AK), and Radial Kurtosis (RK); Axonal Water Fraction (AWF) and Tortuosity (Tort) of the extra-axonal space [33].

- **NODDI indices** [50] — Neurite Density (ND) and Orientation Dispersion Index (ODI).

- **indices computed with MAPL** [34] — Return to Origin (RTOP), Axis (RTAP), and Plane Probability (RTPP); Mean Squared Displacement (MSD), Q-space Inverse Variance (QIV), Non-Gaussianity (NG), and parallel and perpendicular Non-Gaussianity ($NG_{\parallel}$ and $NG_{\perp}$, respectively)[3].

We computed the above metrics in all voxels containing one or more streamlines connecting our pairs of endpoints. Next, we ran the MRtrix implementation of the SIFT2 algorithm [51] in order to assess a contribution of each such streamline and, with those in hand, we computed weighted averages of the microstructure indices.

Our approach in this regard was strictly data-driven. We applied stepwise regression method [52] on the full set of indices for a feature selection. Also, we arranged the streamlines in ascending order with respect to their lengths and tested various subsets of streamlines restricted with low-pass and high-pass filters with cut-off values defined by percentiles of lengths $p_{lower}, p_{upper} \in \{0, 10, 20, \ldots, 100\}$. Note that, particularly, the case of $p_{lower} = p_{upper} = 0$ used no microstructure information at all. We will refer to it as *macrostructure only* and present for comparison.

Having relatively few data, some of which were noisy and incomplete (i.e. Patients 2 and 6), we trained our model with a leave-one-patient-out cross-validation using the data from Patients 1, 3, 4, 5, 7, 8, and 9.

3. Results

Validity of the effective connectivity measurement. Our ECoG recordings were free from significant distortions other than stimulation artifacts. Despite the possible impact of volume-conducted potential [53], we were able to identify N1, P1, and N2 peaks in many recordings, whereas P0 was most often covered by a stimulation artifact. Our cortical responses preserved the variability in timing and strength of response at regions equidistant from the stimulation site, which is not likely to be due to volume conduction, as explained by Keller et al. [19].

All observed N1s occurred between 10 and 60 ms after the onset of DES, with most of them falling into the time interval 20-40 ms (Figure 4a). Note that an incomplete montage of electrodes had a visible impact on the characteristics of recorded N1s. In Patient 2, with $6 + 4 = 10$ electrodes (Table 2), the fraction of early N1s, occurring approximately 20-30 ms after DES, was over-represented with respect to all the other cases (Figure 4a). Also, the range of amplitudes was much narrower for this patient, as well as for Patient 6 with $4 + 4 = 8$ electrodes (Figure 4b).

From the length-based perspective, the distances between stimulation sites and recording electrodes, measured either as shortest streamline lengths or WM surface distances, spread between 10 and 130 mm, whereas median

---

[3]We computed the three Non-Gaussianity indices using diffusion weighted images restricted to those acquired with b-values below 2000 s/mm^2, as suggested by Fick et al. [34].

streamline lengths lied in the range 30-130 mm (Figure 4c-e). These ranges visibly changed after filtering out all the pairs of ROIs for which we did not observe effective connectivity. As a result, mostly the short-distance connections and a few long-distance ones were preserved, suggesting that most of our observed CCEPs traveled along U-fibers. Such modified *min str* and *wm dist* measures peaked at around 20 mm, while most of the *med str* values lied between 60 and 80 mm (Figure 4c-e). We will consider only these filtered macrostructural measures in our correlation analysis below.

[Figure 4 about here.]

Finally, let us note that DES performed during the awake part of a surgery provoked clinical symptoms in all patients. In the representative example of Patient 1, we observed speech arrest, anomia and phonological paraphasias while applying DES in the designated stimulation sites (Figure 5). The presence of such observable symptoms confirmed our choice of stimulation sites and DES parameters for inducing CCEPs.

[Figure 5 about here.]

Correlation of the connectivity measures. The indivdual patient features such as age, sex, pathology type, tumour volume, and presence or absence of epileptic seizures, turned out uncorrelated or very weakly correlated with the propagation of CCEPs (Figure 6). Hence, we disregarded these variables from our study.

[Figure 6 about here.]

We observed a positive correlation between the macrostructural and effective connectivity measures. The Pearson correlation coefficients *r* for the count-based connectivity versus the N1 delays equaled on average 0.51±0.17 (Table 3). In the distance-based measures, the highest *r* coefficients spanned between 0.34 and 0.71 (Table 3). Note that in all cases except for Patient 2, the N1 delays were strongly positively correlated with the shortest streamline lengths. Even though the *wm dist* measure gave relatively high Pearson correlation coefficients in Patients 1 and 3, the remaining scores of *wm dist* were lower, particularly in Patients 2, 4, and 6 (around or below 0.0). The medians of streamline lengths also showed positive correlation with the N1 delays, yet often the lowest among the three distance-based measures, with one notable exception of Patient 2.

We emphasized the role of uncontrollable or partially controllable factors in the experimental setup by providing (in Tables 3 and 4) the four parameters that inevitably influenced our outcomes: current intensity of DES, number of recording electrodes used, number of samples with identified N1 peaks, and average N1 delays/amplitudes with the respective standard deviations. Note that the reduced ECoG montages, composed of 10 or even 8 electrodes (Patients 2 and 6, respectively) delivered fewer data samples than the 14-electrode montages, i.e. 7-9 samples as opposed to 26-44 (Table 3). They also resulted in the shortest observed average N1 delays (about 23-24 ms).

We made analogous observations from the study of correlations between the N1 amplitudes and the macrostructural connectivity measures. In fact, we correlated the square roots of N1 amplitudes with the inverse of minus

9

log-transformed streamlines count $-log\ count^{-1}$ and inverse distances, i.e. $min\ str^{-1}$, $med\ str^{-1}$, and $wm\ dist^{-1}$. We discovered empirically that the N1 amplitudes were rather inversely than directly proportional to the distances, and that the square root function better fitted the above proportion. The Pearson correlation coefficients in the case of N1 amplitudes were lower than the ones in N1 delays. They reached on average 0.37±0.26 for the count-based measures and spanned between 0.32 and 0.79 in the best cases among distance-based measures (Table 4). The inverse *min str* was strongly positively correlated with N1 amplitudes in all the cases except for Patients 3 and 6, which received the lowest current intensities (2.0 and 2.2 mA, respectively). The remaining two distance measures, i.e. *med str* and *wm dist*, most often gave lower Pearson correlation coefficients than *min str*. The role of stimulation parameters was also visible. The N1 amplitudes were larger and more dispersed when the current was relatively high (3.5 mA or above).

[Table 3 about here.]

[Table 4 about here.]

Binary connectivity measures. In this two-class approach, we considered our endpoints as either connected or disconnected. Aiming to find the upper bounds of accuracy between structural and effective connectivity, we sought cut-off thresholds on our structural measures that would maximize accordance with the propagation of CCEPs.

Among the spectrum of potential thresholds, we chose for further study the ones that gave maximum Jaccard index on their respective structural measures. This way, we obtained two-class classifiers of the structural information, reaching the highest agreement with the binary effective connectivity maps, as illustrated for Patient 9 in Figure 7.

The maximum Jaccard index ranged between 0.43 and 0.68 for the log-transformed streamline counts (Table 5), and between 0.39 and 0.74 for the minimum streamline lengths (Table 6). The corresponding sensitivities averaged over all patients equaled to 0.79±0.08 in the case of $-log\ count$ and 0.78±0.07 for *min str*, while specificities were considerably higher reaching 0.92±0.03 and 0.94±0.03, respectively.

Considering the binary structural connectivity matrices referenced to the binary effective ones, the average rate of false positives in the count-based approach was equal to 6±3%, while 4±2% were false negatives (Table 5). In the minimum streamline lengths connectivity (Table 6), the inter-patient averages gave a bit lower percent of false positives (5±2%) and the same percent of false negatives (4±2%) as in the count-based case.

It is worth mentioning that the above false positive and false negative rates corresponded to relatively small brain regions located in the proximity of the stimulation sites. Note that the thresholds that we put on the structural connectivity measures restricted our sets of streamlines to those below 17-55 mm in the count-based approach (Table 5), and 14-24 mm in the length-based approach (Table 6). In other words, our structural measures reached such a good agreement with the CCEP propagation on the streamlines shorter than or equal to the above limits.

[Figure 7 about here.]

[Table 5 about here.]

[Table 6 about here.]

10

Prediction accuracy. The first class of our linear regression models, which used macrostructure information only, produced similar mean residuals for each of the four input measures (Table 7). The root mean squared errors (RMSEs) of N1 delays spanned between 8±9 ms (*min str*) and 9±11 ms (*med str*). Nonetheless, a dispersion of residuals was relatively high. Particularly, when predicting N1 amplitudes, the RMSEs varied from 240±384 µV (−*log count*) to 267±418 µV (*med str*). Variances of the effective connectivity data were best explained by *min str* in the case of N1 delays ($R^2 = 0.11 \pm 0.27$) and −*log count* for N1 amplitudes ($R^2 = 0.06 \pm 0.14$).

The stepwise regression method produced consistent results regarding microstructure features selection (Table 7). Tortuosity of the extra-axonal space was chosen in all the four models aimed at predicting N1 delays. Also, mean and radial kurtosis metrics, non-Gaussianity, and NODDI indices (ND and ODI) appeared repeatedly, while AWF was chosen only once to improve the prediction of N1 delays. Among these metrics: Tort, ND, ODI, and NG increased with the N1 delays, while MK and RK were negatively related.

Analogously, for predicting N1 amplitudes, the stepwise regression method selected FA for −*log count* and *wm dist*, while FA and $NG_\perp$ for *min str* and *med str*. Out of these two metrics: FA was positively, whereas $NG_\perp$ negatively related to the N1 amplitudes.

As we observed, the class of multiple linear regression models, based on a combination of macro- and microstructure data, reached higher prediction accuracy than the one using macrostructure only (Table 7). However, their performance varied depending on the length of streamlines along which the microstructure indices were computed (Figures 8a and 8d). The average R^2 score of the model based on *min str* extended with the microstructure indices visibly increased and became less dispersed after filtering out the shorter half of streamlines (Figure 8). Interestingly, the R^2 rose much more for N1 delays (reaching 0.33±0.09) than for N1 amplitudes (0.12±0.19), which suggests that our microstructure metrics better captured the variability in conduction velocity than the signal decay.

Finally, let us point out that the *macrostructure only* models visibly overestimated the low values of N1 delays and N1 amplitudes, yet understimated the high ones (Figures 8b and 8e). An inclusion of the microstructure indices helped reduce this bias to some extent (Figures 8c and 8f).

[Figure 8 about here.]

[Table 7 about here.]

4. Discussion

We found a large accordance between the structural and effective connectivity measures in brain tumor patients and showed a contribution of microstructure indices in explaining the cortico-cortical transmission. Particularly, the CCEPs that we recorded instrasurgically were linearly related to the indices quantifying axon dispersion and WM tissue composition, which we discuss further in this section.

Our study adds to the growing evidence that the propagation of CCEPs corresponds with the structure of WM bundles [17, 18, 19, 20, 24, 13].

11

4.1. Large accordance between structural and effective connectivity measures

We observed a positive correlation between the structural connectivity measures and the propagation of CCEPs quantified as delays and amplitudes of the N1 peaks. The Pearson correlation coefficients r equaled on average 0.54±0.13 (for N1 delays) and 0.47±0.23 (for N1 amplitudes).

Our results were solid compared to the other approaches described in the literature. In a similar study conducted on epileptic patients, Parker et al. [13] obtained values of r between 0.05 and 0.21 when correlating the absolute amplitudes of CCEPs with the normalized streamline counts between endpoints in the frontal and/or temporal lobes. However, their areas of interests were considerably larger than ours due to the use of grids rather than strips of electrodes. In many of our patients, the size of brain cortex exposed during a surgery would not allow to place grids.

In an animal experiment, van den Heuvel et al. [43] correlated the log-transformed streamline counts from in vivo dMRI scans of macaque brains with two tracer-based connectivity atlases, reaching an accordance of $0.25 \leq r \leq 0.31$. In the mouse brains, Calabrese et al. [44] compared the tractography-based structural connectivity with the tracer data on three levels of granularity. The authors obtained the Spearman correlation coefficients of 0.42 on fine-grained ROIs, 0.71 on midle-sized ROIs, and 0.99 on coarse-grained ROIs ($p \ll 0.05$ in all cases). However, the voxel-wise colocalization revealed rather weak correlation (0.23 ± 0.11) between neuronal tracer and probabilistic tractography. Also note that Spearman and Pearson correlation coefficients are defined differently and as such they cannot be compared directly.

4.2. Double role of the binary connectivity experiment

In our binary approach, we sought the highest agreement between the structural and effective connectivity measures in distinguishing connected from disconnected regions. This experiment allowed us to address two issues that we will discuss below:

4.2.1. Can binary effective connectivity help validate tractography?

Major criticism concerning tractography focuses on its tendency to produce false connections [1, 2, 3, 4]. Even 36±17% of streamlines generated by contemporary algorithms may link regions that are not actually connected [1]. Our binary connectivity experiment indicated 6±3% of false positive and 4±2% of false negative connections when comparing the log-transformed streamline counts with the propagation of CCEPs.

It is tempting to consider the CCEP-based effective connectivity as a method to minimize a fraction of false positive structural links. Note that effectively connected and effectively disconnected regions seem natural candidates as a reference measure of connectivity for tractography [35]. However, one must be aware of the flaws associated to tracing CCEPs. Our study showed that lower current intensities of DES (about 2.0-2.5 mA) came with lower N1 amplitudes and smaller numbers of effective connections found. This implied that the CCEP-based connectivity was more reliable when identifying false negatives than false positives. Indeed, a missing structural link between two effectively connected regions was very likely to exist (a false negative scenario), whereas a lack of effective connectivity between

two regions joined with a streamline might not necessarily mean a false positive, yet also be caused by wrong DES parameters, low signal to noise ratio in ECoG recordings, or an interference with other electrophysiological activities.

Jeurissen et al. [2] claimed recently that tractography required filtering methods to decrease the rates of false positives. We believe that CCEP could deliver crucial priors in this regard, although the methodology related to recording and tracing the effective connectivity induced by DES still needs improvements.

4.2.2. Which structural connectivity is needed to ensure effective connectivity?

It is known that DES of the brain cortex primarily affects pyramidal cells at the stimulation site [19]. However, the propagation of CCEPs towards the target pyramidal cells through WM and its relation to the structural connectivity are still not sufficiently studied [19, 24]. For instance, it is not clear whether some measures of structural connectivity can discriminate between effectively connected and effectively disconnected regions. And if so, then where is the structural borderline between these two classes?

Matsumoto et al. [17] and Yamao et al. [20] observed long-ranged effective connectivity between anterior and posterior perisylvian language areas. On the contrary, the propagation of CCEPs in our experiments was mostly local. It is worth noticing that in their experiment the current intensities ranged from 10 to 15 mA and the stimulating electrode had a 10-mm distance between poles, as opposed to 2-5 mA and 5-mm distance in our case. According to Vincent et al. [28], these two variables mostly affect the scope of DES. We thus believe that it is more appropriate to determine structural boundaries of the effective connectivity given certain DES parameters.

In our binary connectivity experiments, highest agreement between the structural and effective measures was reached when the streamline count-based probability surpassed 0.009±0.004 or when the shortest streamline lengths remained below 20±3 mm, which roughly approximated the limits of effective connectivity in terms of the structural measures. Additionally, this suggests that our CCEPs might have traveled along U-fibers rather than long fascicles like AF, since the typical lengths of the former lie between 3 and 30 mm [54].

4.3. Prediction of CCEP propagation with structural connectivity measures

The type and strength of correlation between the studied structural and effective connectivity measures suggested that we might predict the CCEP propagation by applying linear regression on the structure-based variables. Indeed, the residuals of the proposed prediction models were relatively low on average, although somewhat dispersed.

Our experiments showed that the linear regression of the log-transformed streamline counts or the minimum streamline lengths reached higher accuracy than the one based on *med str* or *wm dist*. It is then very likely that our CCEPs traveled along the shortest structural links between the endpoints rather than long-range fibers. Interestingly, the fact that *min str* outperformed *wm dist* in this comparison suggests that the trajectory from a stimulation site to a recording electrode as measured on the WM surface was not accurate enough to capture the CCEP propagation pattern. This supports the argument of communication via U-fibers, advocated by Conner et al. [18], rather than the impact of volume-conducted potential signalized recently in the literature [53].

13

In this work, we hypothesized that the propagation of CCEPs, measured as a spatial accumulation of N1 delays and a decay of N1 amplitudes, may implicitly relate to the properties of neuronal tissue connecting the source and target pyramidal cells. The observed increase of the R^2 score and decrease of its dispersion after including the microstructure-related indices in our linear regression models imply tangibly that these indices contained information related to CCEPs.

As a matter of fact, neural conduction largely depends on axon diameter, myelin sheath thickness and axonal membrane properties [30], however an approximation of these microstructural features is challenging in vivo [31, 34, 55, 56, 57]. One solution is to capture them through non-specific markers that quantify the tissue composition [58]. For instance, FA was already shown to correlate with conduction velocity [22] and functional connectivity [59]. In this work, we considered FA and other DTI-based indices, i.e. MD, RD, and AD, which often serve as surrogate measures of tissue microstructure [50, 31]. In addition, we included the metrics of DKI-based quantification of non-Gaussian diffusion, namely MK, RK, and AK, whose clinical significance has been shown in relation to the age-related demyelination [60] and brain tumour staging [61]. Simultaneously, Sen and Basser [30] argued that tortuosity of the extra-axonal space, which also can be quantified with DKI [33], limits the conduction in a restrictive geometry of fibers.

Numerous microstructure features with known impact on conduction velocity provide more specific information, although require longer acqusition than DTI or DKI. Jespersen et al. [62] showed that neurite density estimates correlated with the myelination level, which led us to include the NODDI-based indices of ND and ODI derived from our multi-shell acquisition. The use of MAPL signal representation allowed us to incorporate a group of less common indices of tissue composition like QIV, considered more sensible than FA [63], or NG. Surprisingly, RTOP, RTAP, and RTPP, belonging to the group of indices typically atributed to volume, cross-sectional area, and length of pores (respectively) [39, 34] turned out less significant than other indices in our study.

On the other hand, the presence of FA and tortuosity among the features selected with our stepwise regression is by far the most intuitive. The impact of both these metrics is consistent with the previous reports [30, 22], similarly to ND and ODI, as we mentioned earlier. Interestingly, the N1 delays, reflecting de facto the conduction velocity, appeared visibly more related to the studied microstructure indices than the N1 amplitudes. The latter apparently decayed proportionally to the streamline lengths and counts, although maintained the variability that we were unable to explain with the WM microstructure. Alternative approaches to weighting the q-space indices or filtering tracts could probably improve those results.

5. Conclusions

In this work, we studied the relation between the structural connectivity measures obtained from dMRI and the effective connectivity measures based on the propagation of CCEPs in the brain tumor patients. Our experiments showed positive correlation between streamline lengths and counts with the delays and amplitudes of N1 peaks.

When comparing the binary variants of the structural and effective brain connectivity, we discussed the potential of CCEPs to filter out the results of tractography and estimated the structural criteria of the CCEP propagation. Finally, we showed that brain tissue microstructure features help explain the propagation of CCEPs. The N1 delays and N1 amplitudes measured instrasurgically were linearly related to the indices quantifying axon dispersion and WM tissue composition. Particularly, the tortuosity of the extra-axonal space, mean and radial kurtosis, and neurite density indices considerably improved the prediction of effective connectivity measures. We believe that our findings extend the clinical significance of microstructure indices and contribute to the goal of understanding the propagation of CCEPs.

Acknowledgements

References

[1] K. H. Maier-Hein, P. F. Neher, J.-C. Houde, M.-A. Côté, E. Garyfallidis, J. Zhong, M. Chamberland, F.-C. Yeh, Y.-C. Lin, Q. Ji, et al., The challenge of mapping the human connectome based on diffusion tractography, Nature communications 8 (2017) 1349.

[2] B. Jeurissen, M. Descoteaux, S. Mori, A. Leemans, Diffusion mri fiber tractography of the brain, NMR in Biomedicine 32 (2019) e3785.

[3] D. K. Jones, Challenges and limitations of quantifying brain connectivity in vivo with diffusion mri, Imaging in Medicine 2 (2010) 341–355.

[4] C. Thomas, Q. Y. Frank, M. O. Irfanoglu, P. Modi, K. S. Saleem, D. A. Leopold, C. Pierpaoli, Anatomical accuracy of brain connections derived from diffusion mri tractography is inherently limited, Proceedings of the National Academy of Sciences 111 (2014) 16574–16579.

[5] B. Jeurissen, J.-D. Tournier, T. Dhollander, A. Connelly, J. Sijbers, Multi-tissue constrained spherical deconvolution for improved analysis of multi-shell diffusion mri data, NeuroImage 103 (2014) 411–426.

[6] S. Jbabdi, H. Johansen-Berg, Tractography: where do we go from here?, Brain connectivity 1 (2011) 169–183.

[7] H. Duffau, Lessons from brain mapping in surgery for low-grade glioma: insights into associations between tumour and brain plasticity, The Lancet Neurology 4 (2005) 476–486.

[8] H. Duffau, P. Gatignol, E. Mandonnet, L. Capelle, L. Taillandier, Intraoperative subcortical stimulation mapping of language pathways in a consecutive series of 115 patients with grade ii glioma in the left dominant hemisphere, Journal of neurosurgery 109 (2008) 461–471.

[9] E. Mandonnet, P. A. Winkler, H. Duffau, Direct electrical stimulation as an input gate into brain functional networks: principles, advantages and limitations, Acta neurochirurgica 152 (2010) 185–193.

[10] G. A. Ojemann, Brain organization for language from the perspective of electrical stimulation mapping, Behavioral and Brain Sciences 6 (1983) 189–206.

[11] W. Penfield, E. Boldrey, Somatic motor and sensory representation in the cerebral cortex of man as studied by electrical stimulation, Brain 60 (1937) 389–443.

[12] K. J. Friston, Functional and effective connectivity: a review, Brain connectivity 1 (2011) 13–36.

[13] C. S. Parker, J. D. Clayden, M. J. Cardoso, R. Rodionov, J. S. Duncan, C. Scott, B. Diehl, S. Ourselin, Structural and effective connectivity in focal epilepsy, NeuroImage: Clinical 17 (2018) 943–952.

[14] G. E. Keles, M. S. Berger, Advances in neurosurgical technique in the current management of brain tumors, in: Seminars in oncology, volume 31, Elsevier, pp. 659–665.

[15] P. D. W. Hamer, S. G. Robles, A. H. Zwinderman, H. Duffau, M. S. Berger, Impact of intraoperative stimulation brain mapping on glioma surgery outcome: a meta-analysis, J Clin Oncol 30 (2012) 2559–2565.

[16] M. Vigneau, V. Beaucousin, P.-Y. Herve, H. Duffau, F. Crivello, O. Houde, B. Mazoyer, N. Tzourio-Mazoyer, Meta-analyzing left hemisphere language areas: phonology, semantics, and sentence processing, Neuroimage 30 (2006) 1414–1432.

[17] R. Matsumoto, D. R. Nair, E. LaPresto, I. Najm, W. Bingaman, H. Shibasaki, H. O. Lüders, Functional connectivity in the human language system: a cortico-cortical evoked potential study, Brain 127 (2004) 2316–2330.

[18] C. R. Conner, T. M. Ellmore, M. A. DiSano, T. A. Pieters, A. W. Potter, N. Tandon, Anatomic and electro-physiologic connectivity of the language system: a combined dti-ccep study, Computers in biology and medicine 41 (2011) 1100–1109.

[19] C. J. Keller, C. J. Honey, P. Mégevand, L. Entz, I. Ulbert, A. D. Mehta, Mapping human brain networks with cortico-cortical evoked potentials, Phil. Trans. R. Soc. B 369 (2014) 20130528.

[20] Y. Yamao, R. Matsumoto, T. Kunieda, Y. Arakawa, K. Kobayashi, K. Usami, S. Shibata, T. Kikuchi, N. Sawamoto, N. Mikuni, et al., Intraoperative dorsal language network mapping by using single-pulse electrical stimulation, Human brain mapping 35 (2014) 4345–4361.

[21] C. Büchel, K. J. Friston, Effective connectivity and neuroimaging, SPMcourse, short course notes (1997).

[22] B. H. Silverstein, E. Asano, A. Sugiura, M. Sonoda, M.-H. Lee, J.-W. Jeong, Dynamic tractography: Integrating cortico-cortical evoked potentials and diffusion imaging, NeuroImage (2020) 116763.

[23] K. Terada, S. Umeoka, N. Usui, K. Baba, K. Usui, S. Fujitani, K. Matsuda, T. Tottori, F. Nakamura, Y. Inoue, Uneven interhemispheric connections between left and right primary sensori-motor areas, Human brain mapping 33 (2012) 14–26.

[24] R. Matsumoto, T. Kunieda, D. Nair, Single pulse electrical stimulation to probe functional and pathological connectivity in epilepsy, Seizure 44 (2017) 27–36.

[25] M. Vincent, F. Bonnetblanc, E. Mandonnet, A. Boyer, H. Duffau, D. Guiraud, Measuring the electrophysiological effects of direct electrical stimulation after awake brain surgery, Journal of Neural Engineering 17 (2020) 016047.

[26] A. Boyer, H. Duffau, M. Vincent, S. Ramdani, E. Mandonnet, D. Guiraud, F. Bonnetblanc, Electrophysiological activity evoked by direct electrical stimulation of the human brain: interest of the p0 component, in: 2018 40th annual international conference of the IEEE engineering in medicine and biology society (EMBC), IEEE, pp. 2210–2213.

[27] G. Alarcón, J. Martinez, S. V. Kerai, M. E. Lacruz, R. Q. Quiroga, R. P. Selway, M. P. Richardson, J. J. G. Seoane, A. Valentín, In vivo neuronal firing patterns during human epileptiform discharges replicated by electrical stimulation, Clinical Neurophysiology 123 (2012) 1736–1744.

[28] M. Vincent, D. Guiraud, H. Duffau, E. Mandonnet, F. Bonnetblanc, Electrophysiological brain mapping: Basics of recording evoked potentials induced by electrical stimulation and its physiological spreading in the human brain, Clinical Neurophysiology 128 (2017) 1886–1890.

[29] O. David, A.-S. Job, L. De Palma, D. Hoffmann, L. Minotti, P. Kahane, Probabilistic functional tractography of the human cortex, Neuroimage 80 (2013) 307–317.

[30] P. N. Sen, P. J. Basser, A model for diffusion in white matter in the brain, Biophysical journal 89 (2005) 2927–2938.

[31] P. J. Basser, C. Pierpaoli, Microstructural and physiological features of tissues elucidated by quantitative-diffusion-tensor mri, Journal of magnetic resonance 213 (2011) 560–570.

[32] J. H. Jensen, J. A. Helpern, Mri quantification of non-gaussian water diffusion by kurtosis analysis, NMR in Biomedicine 23 (2010) 698–710.

[33] E. Fieremans, J. H. Jensen, J. A. Helpern, White matter characterization with diffusional kurtosis imaging, Neuroimage 58 (2011) 177–188.

[34] R. H. Fick, D. Wassermann, E. Caruyer, R. Deriche, Mapl: Tissue microstructure estimation using laplacian-regularized map-mri and its application to hcp data, NeuroImage 134 (2016) 365–385.

[35] L. Trebaul, P. Deman, V. Tuyisenge, M. Jedynak, E. Hugues, D. Rudrauf, M. Bhattacharjee, F. Tadel, B. Chanteloup-Foret, C. Saubat, et al., Probabilistic functional tractography of the human cortex revisited, NeuroImage 181 (2018) 414–429.

[36] NIH U.S. National Library of Medicitne, Clinicaltrials.gov website, https://clinicaltrials.gov/ct2/show/NCT03503110, 2009.

[37] ConnecTC, Zenodo.org website, `https://doi.org/10.5281/zenodo.3989987`, 2020.

[38] A. Szelényi, L. Bello, H. Duffau, E. Fava, G. C. Feigl, M. Galanda, G. Neuloh, F. Signorelli, F. Sala, Intraoperative electrical stimulation in awake craniotomy: methodological aspects of current practice, Neurosurgical focus 28 (2010) E7.

[39] E. Özarslan, C. G. Koay, T. M. Shepherd, M. E. Komlosh, M. O. İrfanoğlu, C. Pierpaoli, P. J. Basser, Mean apparent propagator (MAP) MRI: A novel diffusion imaging method for mapping tissue microstructure, NeuroImage 78 (2013) 16–32.

[40] J. D. Tournier, F. Calamante, A. Connelly, Improved probabilistic streamlines tractography by 2nd order integration over fibre orientation distributions, in: Proceedings of the international society for magnetic resonance in medicine, volume 18, Ismrm, p. 1670.

[41] C. Reveley, A. K. Seth, C. Pierpaoli, A. C. Silva, D. Yu, R. C. Saunders, D. A. Leopold, Q. Y. Frank, Superficial white matter fiber systems impede detection of long-range cortical connections in diffusion mr tractography, Proceedings of the National Academy of Sciences 112 (2015) E2820–E2828.

[42] E. Garyfallidis, M. Brett, B. Amirbekian, A. Rokem, S. Van Der Walt, M. Descoteaux, I. Nimmo-Smith, Dipy, a library for the analysis of diffusion mri data, Frontiers in neuroinformatics 8 (2014) 8.

[43] M. P. van den Heuvel, M. A. de Reus, L. Feldman Barrett, L. H. Scholtens, F. M. Coopmans, R. Schmidt, T. M. Preuss, J. K. Rilling, L. Li, Comparison of diffusion tractography and tract-tracing measures of connectivity strength in rhesus macaque connectome, Human brain mapping 36 (2015) 3064–3075.

[44] E. Calabrese, A. Badea, G. Cofer, Y. Qi, G. A. Johnson, A diffusion mri tractography connectome of the mouse brain and comparison with neuronal tracer data, Cerebral cortex 25 (2015) 4628–4637.

[45] B. Fischl, Freesurfer, Neuroimage 62 (2012) 774–781.

[46] M. A. de Reus, M. P. van den Heuvel, Estimating false positives and negatives in brain networks, Neuroimage 70 (2013) 402–409.

[47] I. Tasaki, T. Takeuchi, Der am ranvierschen knoten entstehende aktionsstrom und seine bedeutung für die erregungsleitung, Pflügers Archiv European Journal of Physiology 244 (1941) 696–711.

[48] W. Rushton, A theory of the effects of fibre size in medullated nerve, The Journal of physiology 115 (1951) 101–122.

[49] L. Goldman, J. S. Albus, Computation of impulse conduction in myelinated fibers; theoretical basis of the velocity-diameter relation, Biophysical journal 8 (1968) 596–607.

[50] H. Zhang, T. Schneider, C. A. Wheeler-Kingshott, D. C. Alexander, Noddi: practical in vivo neurite orientation dispersion and density imaging of the human brain, Neuroimage 61 (2012) 1000–1016.

[51] R. E. Smith, J.-D. Tournier, F. Calamante, A. Connelly, Sift2: Enabling dense quantitative assessment of brain white matter connectivity using streamlines tractography, Neuroimage 119 (2015) 338–351.

[52] M. Efroymson, Multiple regression analysis, Mathematical methods for digital computers (1960) 191–203.

[53] S. Shimada, N. Kunii, K. Kawai, T. Matsuo, Y. Ishishita, K. Ibayashi, N. Saito, Impact of volume-conducted potential in interpretation of cortico-cortical evoked potential: Detailed analysis of high-resolution electrocorticography using two mathematical approaches, Clinical Neurophysiology 128 (2017) 549–557.

[54] A. Schüz, R. Miller, Cortical areas: unity and diversity, CRC Press, 2002.

[55] Y. Assaf, T. Blumenfeld-Katzir, Y. Yovel, P. J. Basser, Axcaliber: a method for measuring axon diameter distribution from diffusion MRI, Magnetic Resonance in Medicine: An Official Journal of the International Society for Magnetic Resonance in Medicine 59 (2008) 1347–1354.

[56] E. Özarslan, P. J. Basser, Microscopic anisotropy revealed by NMR double pulsed field gradient experiments with arbitrary timing parameters, The Journal of chemical physics 128 (2008) 04B615.

[57] J. Veraart, D. Nunes, U. Rudrapatna, E. Fieremans, D. K. Jones, D. S. Novikov, N. Shemesh, Noninvasive quantification of axon radii using diffusion mri, Elife 9 (2020) e49855.

[58] C. Pierpaoli, P. Jezzard, P. J. Basser, A. Barnett, G. Di Chiro, Diffusion tensor MR imaging of the human brain., Radiology 201 (1996) 637–648.

[59] E. D. Boorman, J. O'Shea, C. Sebastian, M. F. Rushworth, H. Johansen-Berg, Individual differences in white-matter microstructure reflect variation in functional connectivity during choice, Current Biology 17 (2007) 1426–1431.

[60] M. F. Falangola, J. H. Jensen, J. S. Babb, C. Hu, F. X. Castellanos, A. Di Martino, S. H. Ferris, J. A. Helpern, Age-related non-gaussian diffusion patterns in the prefrontal brain, Journal of Magnetic Resonance Imaging: An Official Journal of the International Society for Magnetic Resonance in Medicine 28 (2008) 1345–1350.

[61] P. Raab, E. Hattingen, K. Franz, F. E. Zanella, H. Lanfermann, Cerebral gliomas: diffusional kurtosis imaging analysis of microstructural differences, Radiology 254 (2010) 876–881.

[62] S. N. Jespersen, C. R. Bjarkam, J. R. Nyengaard, M. M. Chakravarty, B. Hansen, T. Vosegaard, L. Østergaard, D. Yablonskiy, N. C. Nielsen, P. Vestergaard-Poulsen, Neurite density from magnetic resonance diffusion measurements at ultrahigh field: comparison with light microscopy and electron microscopy, Neuroimage 49 (2010) 205–216.

[63] R. H. J. Fick, M. Pizzolato, D. Wassermann, M. Zucchelli, G. Menegaz, R. Deriche, A sensitivity analysis of q-space indices with respect to changes in axonal diameter, dispersion and tissue composition, in: 2016 IEEE 13th International Symposium on Biomedical Imaging (ISBI), IEEE, pp. 1241–1244.

List of Figures

Figure 1: A schematic shape of a Cortico-Cortical Evoked Potential, which typically consists of four consecutive voltage peaks named P1, N1, P2, and N2, where N are negative peaks while P are positive ones. An alternative naming convention is also used in the literature, according to which the positive peaks are enumerated from zero, hence P0 and P1 (in parentheses). The plot conforms to the commonly used convention of drawing ECoG recordings with the reversed y-axis.
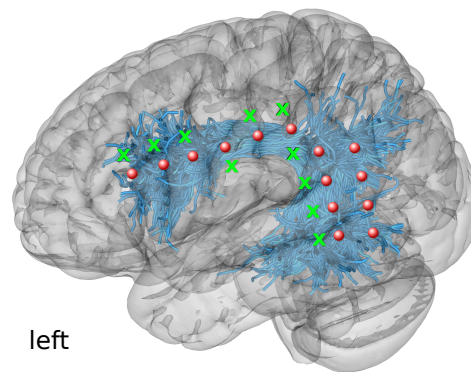
(a) presurgical planning
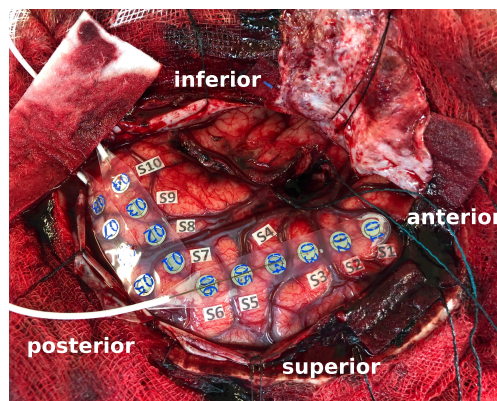
(b) intrasurgical scene

Figure 2: ECoG electrodes for recording CCEPs in Patient 7: (a) presurgical planning of the locations of electrodes (red circles) and stimulation sites (green crosses) using the tractography-based dissections of Arcuate Fasciculus and Superior Longitudinal Fasciculus III (both pictured jointly as blue streamlines), (b) intrasurgical positions of the ECoG electrodes and the stimulation sites (marked with labels S1-S10).
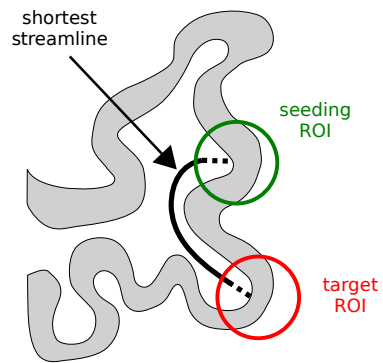
Figure 3: Sample spherical ROIs surrounding two endpoints — a stimulation site (seeding ROI) and an ECoG electrode location (target ROI). The shortest streamline (showed as thick black line) found between them by a tractography algorithm begins and terminates near the boundaries of the spheres, which leads to underestimation of the streamline's length. As a compensation, the streamline's length is increased with the average distances to the centers of ROIs, as illustrated with dotted lines.
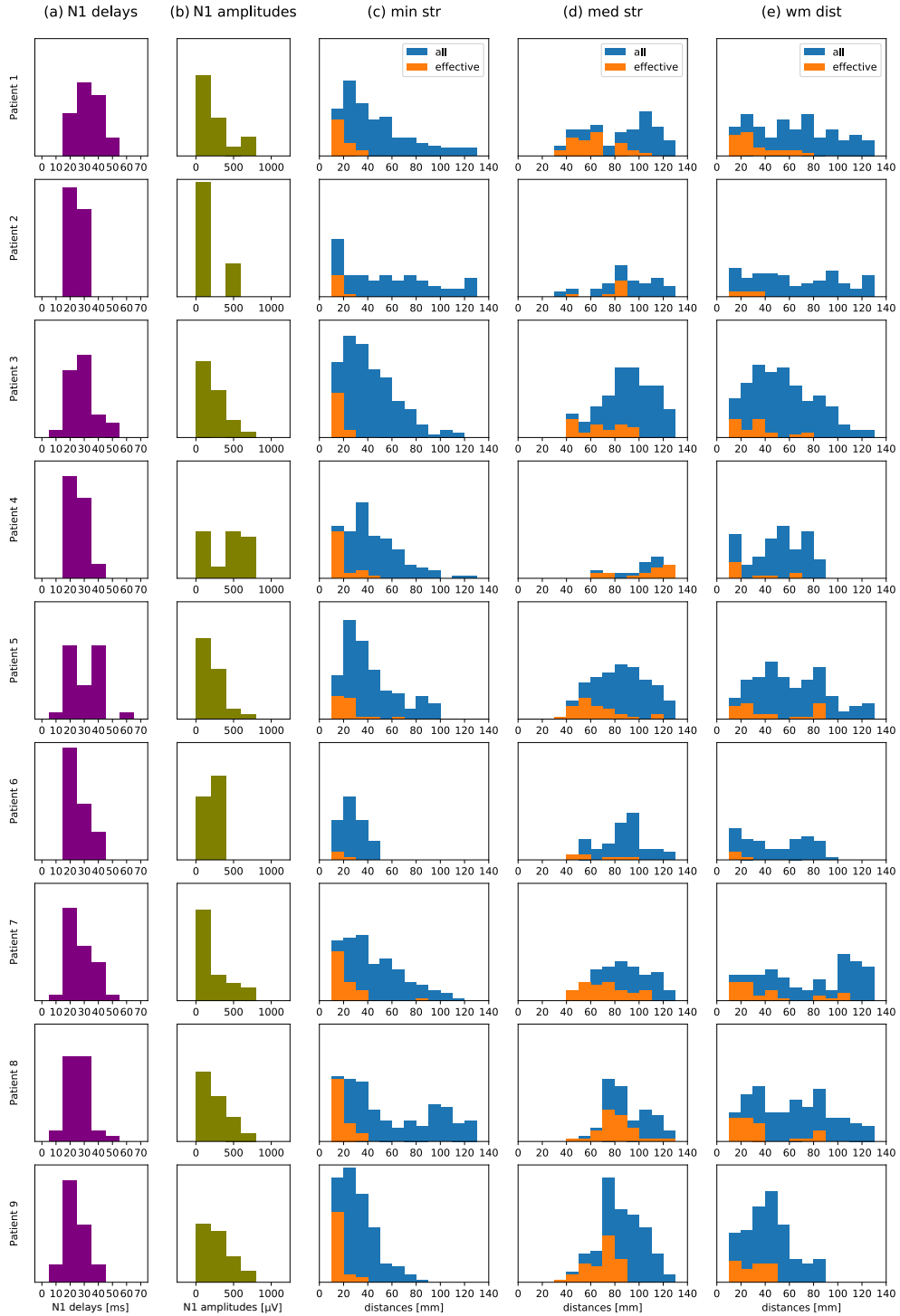
Figure 4: In most of the cases, CCEPs emerged 20-40 ms after the stimulation onset and propagated 10-60 mm away from the stimulation sites. The first two columns present the histograms of (a) delays and (b) amplitudes of N1 peaks. The remaining three columns show the histograms of our macrostructural measures: (c) minimum and (d) median lengths of dMRI-based streamlines connecting source and target ROIs, and (e) distances between the respective pairs of ROIs measured along the white matter surface. The histograms in blue present all structural connections, while the ones in orange refer to those among the structural connections for which we observed propagation of CCEPs (effective connectivity).
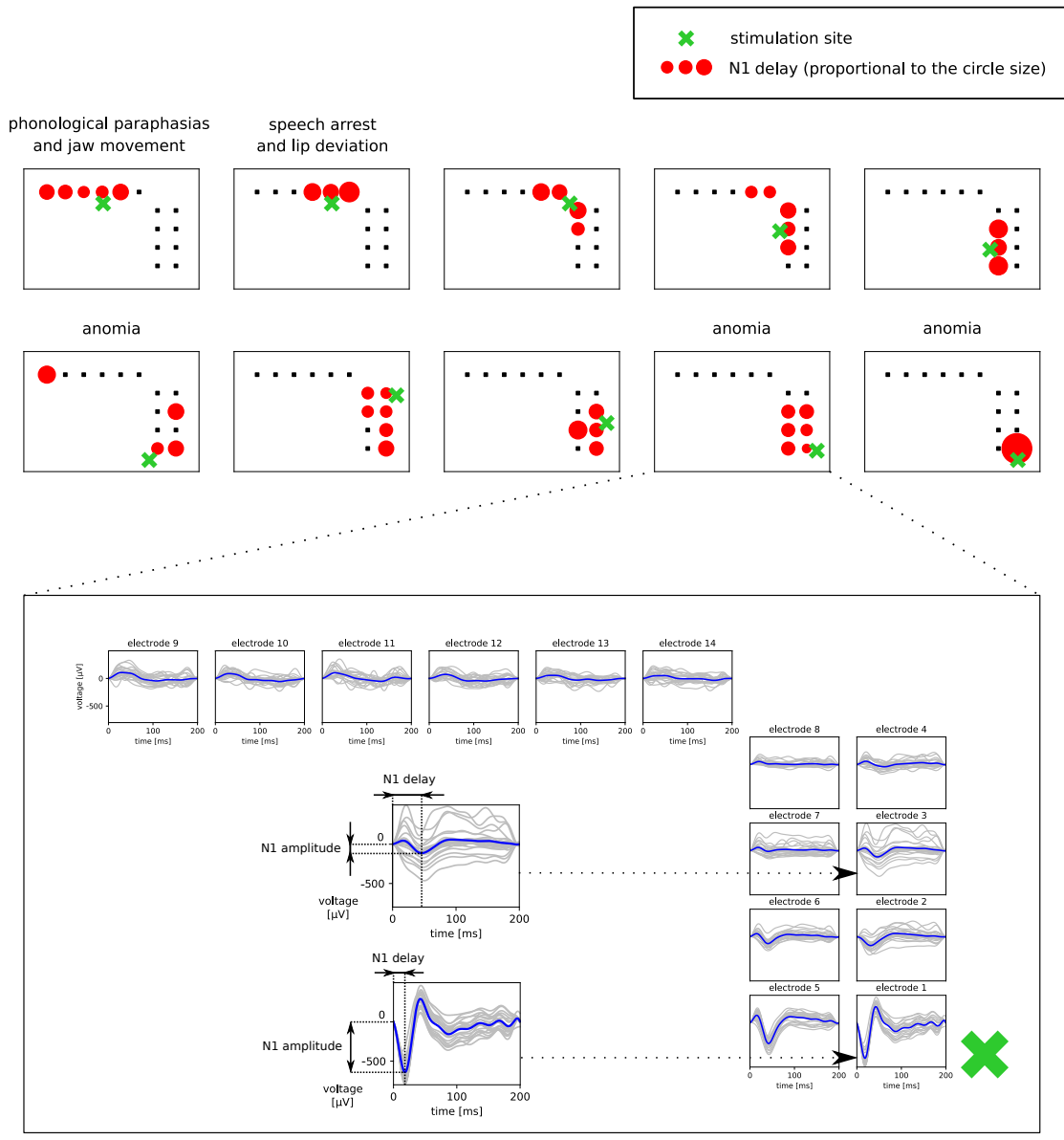
Figure 5: Recorded propagation of CCEPs while applying DES to Patient 1. All plots illustrate the locations of the 6-electrode strip and the two parallel 4-electrode strips placed on the cortex. The schemes given at the top present the clinical symptoms, observed when applying DES, and the propagation of CCEPs from each of the stimulation sites (green crosses) shown as N1 delays (quantities are proportional to the diameter of the red circles) or tiny black boxes marking the electrodes where we observed no N1. The field at the bottom shows a sample denoised ECoG signal acquired during electrical stimulation as seen before (gray plots) and after averaging of event epochs (blue plots). The two zoomed plots show the N1 delays and N1 amplitudes recorded in the proximity of the stimulation (lower plot) and distally (upper plot).
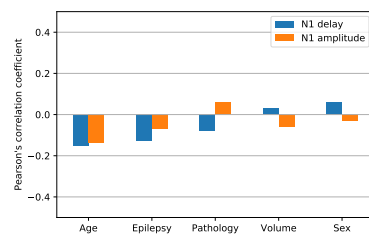
Figure 6: Indivdual patient features such as age, sex, pathology type, tumour volume, and presence or absence of epileptic seizures, turned out uncorrelated or very weakly correlated with the propagation of CCEPs measured as N1 delays and amplitudes.
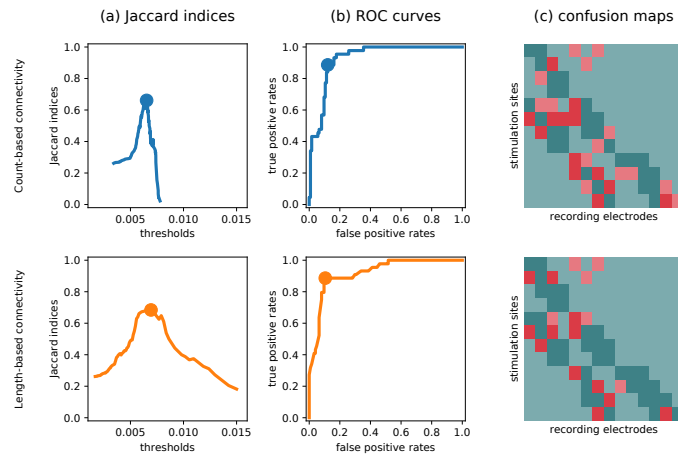
Figure 7: A comparison of the structural and effective brain connectivity measures at the binary level allowed to assess the structural thresholds above which CCEPs were observed and approximate the rate of false positives among selected tractography results. Column (a) shows Jaccard indices computed for all possible tresholds on the count-based (top row) and the length-based (bottom row) binary structural connectivity in Patient 9. The maximum (marked with a filled circle) is reached at 0.007, which means that a high-pass filter with the cut-off value 0.007 ensures highest agreement between the structural and effective connectivities. The associated ROC curves are presented in column (b), while column (c) shows the confusion maps. In the latter, dark green squares represent true positives, light green — true negatives, dark red — false positives, and light red — false negatives.

Prediction of N1 delays

(a) R^2 scores

(b) macrostructure only (Bland-Altman plot)

(c) macro- and microstructure (B.-A. plot)

Prediction of N1 amplitudes

(d) R^2 scores

(e) macrostructure only (B.-A. plot)

(f) macro- and microstructure (B.-A. plot)
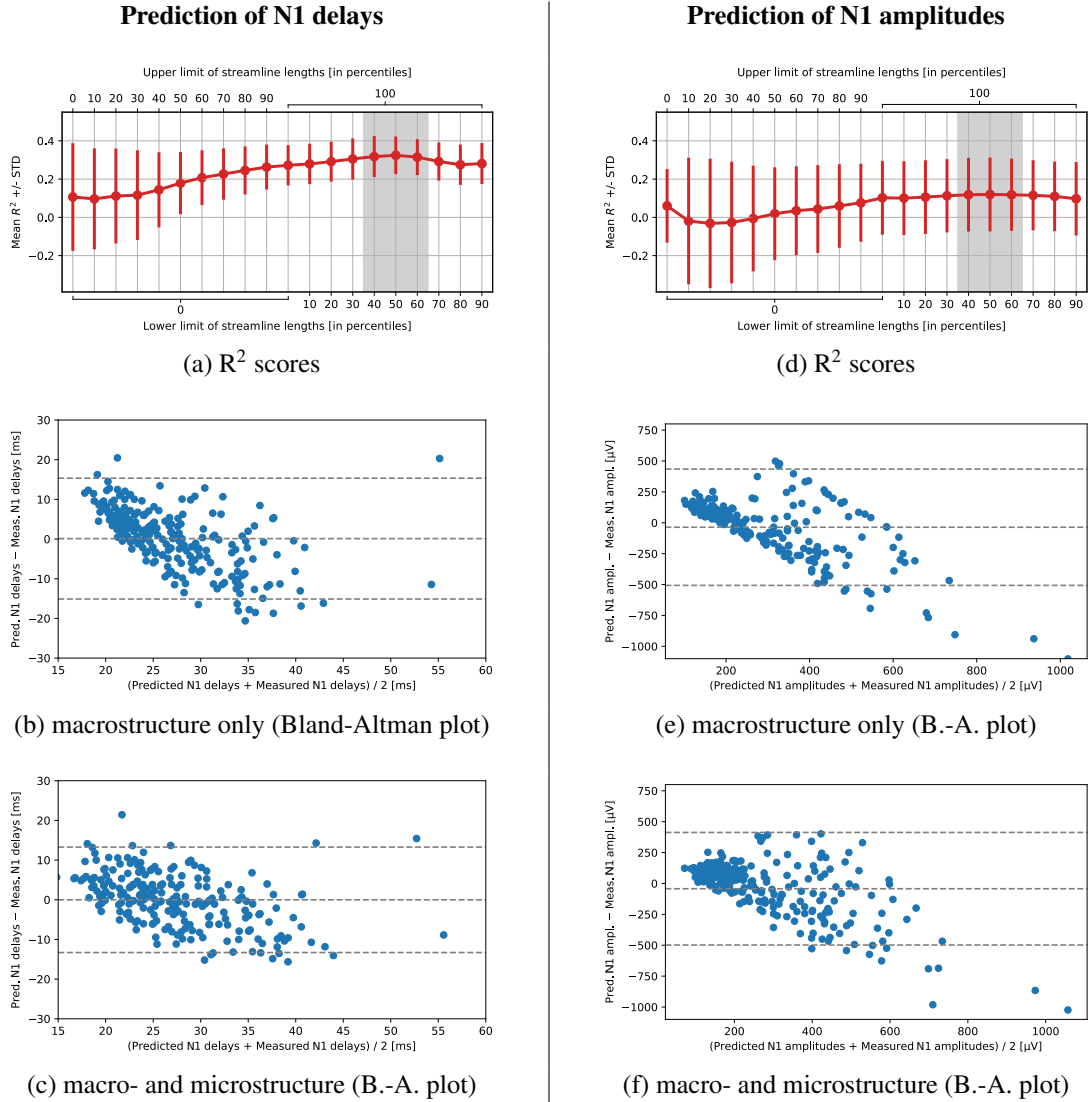
Figure 8: The accuracy of prediction visibly depended on the lengths of streamlines used for computing microstructure information, especially in the case of N1 delays. To account for that, the shortest and the longest streamlines were filtered out. The respective low- and high-pass filters were defined by the percentiles of lengths $p_{lower}, p_{upper} \in \{0, 10, 20, \dots, 100\}$. The mean R^2 scores with standard deviations for various lower and upper cut-off values are shown for N1 delays (a) and N1 amplitudes (d). Note that the *macrostructure only* case is defined with $p_{lower} = p_{upper} = 0$. The areas of best scores around $p_{lower} = 50, p_{upper} = 100$ are highlighted. The four remaining figures are Bland-Altman (B.-A.) plots illustrating the prediction accuracy obtained with the leave-one-patient-out cross-validation for the *macrostructure only* cases (b and e) or *macro- and microstructure* cases with best cut-off values, i.e. $p_{lower} = 50, p_{upper} = 100$ (c and f). In each of the four plots, an overestimation of low values and an underestimation of high values is seen, however the cases with the microstructure information included partially compensated this bias.

29

patient	age	sex	pathology	location	volume	epilepsy	drug	history
1	46	M	cavernous angioma	occipital (L)	3 cm^3	N	levetiracetam 500mg, 2x / day	—
2	38	F	glioblastoma IDH wildtype (IV)	fronto-opercular (L)	12 cm^3	Y (partial)	levetiracetam 500mg, 2x / day	—
3	25	F	glioblastoma IDH mutant (IV)	frontal (L)	110 cm^3	N	levetiracetam 500mg, 2x / day	—
4	41	M	astrocytoma IDH mutant (II)	fronto-temporo--insular (R)	162 cm^3	Y (generalized)	levetiracetam 1000mg, 2x / day	—
5	35	F	oligodendroglioma IDH mutant (II)	frontal (L)	88 cm^3	Y (generalized)	levetiracetam 500mg, 2x / day	—
6	32	M	astrocytoma IDH mutant (II)	temporal (L)	5 cm^3	N	levetiracetam 500mg, 2x / day	chemotherapy PCV (4 cycles)
7	23	F	oligodendroglioma IDH mutant (II)	temporo-insular (L)	77 cm^3	Y (partial)	levetiracetam 500mg, 2x / day	—
8	51	M	astrocytoma IDH wildtype (III)	temporal (L)	26 cm^3	Y (generalized)	levetiracetam 500mg, 2x / day	—
9	66	F	glioblastoma IDH wildtype (IV)	supplementary motor area (L)	8 cm^3	Y (partial)	levetiracetam 500mg, 2x / day	—

Table 1: Summary of patients data including type, location, and volume of the pathology (II, III, IV — WHO grades; L, R — left / right brain hemisphere), epilepsy, antiepileptic drug administered, and the history of previous anticancer treatment.

patient	stimulation parameters				acquisition parameters	
	current	frequency	pulse width	sites num	montage of electrodes	sampling rate
1	3.5 mA	5 Hz	1 ms	10	4 + 4 + 6 = 14	2 kHz
2	2.5 mA	2 Hz	1 ms	10	4 + 6 = 10	2 kHz
3	2.0 mA	2 Hz	1 ms	14	4 + 4 + 6 = 14	2 kHz
4	5.0 mA	2 Hz	1 ms	9	4 + 4 + 6 = 14	2 kHz
5	2.5 mA	2 Hz	1 ms	11	4 + 4 + 6 = 14	2 kHz
6	2.2 mA	2 Hz	1 ms	8	4 + 4 = 8	2 kHz
7	5.0 mA	2 Hz	1 ms	10	4 + 4 + 6 = 14	2 kHz
8	5.0 mA	2 Hz	1 ms	10	4 + 4 + 6 = 14	2 kHz
9	5.0 mA	2 Hz	1 ms	10	4 + 4 + 6 = 14	2 kHz

Table 2: Summary of parameters used for the intrasurgical electrical stimulation and the simultaneous acquisition of the ECoG signal in 9 patients. The square waveform of biphasic current was composed of pulses having constant widths of 1 ms each. The stimulation frequency was fixed at 2 Hz in all cases except for Patient 1 having 5 Hz. The current intensities ranged from 2 to 5 mA. The ECoG montages comprised of one or two short strips with 4 electrodes each and/or one longer strip with 6 electrodes, totaling 8, 10, or 14 recording electrodes. The stimulation sites were located in the proximity of accessible electrodes, i.e. all electrodes except for those slipped under the dura matter. Their number is provided as *sites num*. The fixed sampling rate of 2 kHz was used for all acquisitions.

patient	current	electr.	samples	mean delays	N1 delays correlation with			
					−log count	min str	med str	wm dist
1	3.5 mA	14	32	33±9 ms	0.51 (.003)	**0.64 (.001)**	0.31 (.086)	0.57 (.001)
2	2.5 mA	10	9	24±4 ms	0.07 (.865)	0.36 (.346)	**0.56 (.117)**	-0.14 (.710)
3	2.0 mA	14	26	28±9 ms	0.66 (.001)	**0.54 (.004)**	-0.23 (.249)	0.49 (.012)
4	5.0 mA	14	27	26±7 ms	0.58 (.002)	**0.66 (.001)**	-0.29 (.145)	-0.13 (.519)
5	2.5 mA	14	29	29±11 ms	0.69 (.001)	**0.71 (.001)**	0.31 (.105)	0.25 (.189)
6	2.2 mA	8	7	23±8 ms	0.47 (.284)	**0.34 (.462)**	0.21 (.657)	0.09 (.847)
7	5.0 mA	14	36	27±9 ms	0.59 (.001)	**0.60 (.001)**	0.37 (.027)	0.32 (.053)
8	5.0 mA	14	37	25±7 ms	0.42 (.009)	**0.46 (.004)**	0.31 (.066)	0.40 (.013)
9	5.0 mA	14	44	23±7 ms	0.56 (.001)	**0.57 (.001)**	-0.40 (.007)	0.35 (.019)
				average:	0.51±0.17	**0.54±0.13**	0.13±0.32	0.24±0.24

Table 3: The N1 delays were strongly positively correlated with the shortest streamline lengths (*min str*) in most of the cases. The three rightmost columns show the Pearson correlation coefficients *r* computed for the N1 delays paired with the three studied distance measures. The respective p-values are given in parentheses. The highest scores per patient, spanning between 0.34 and 0.71, are printed in bold. Note that a positive correlation was also held for the reciprocal of log-transformed streamline counts (−*log count*). Additionally, in order to emphasize the role of uncontrollable factors in experimental setup, the following are specified: current intensity of DES, number of recording electrodes used, number of samples with N1 peaks identified, and average N1 delays with the respective standard deviations.

					$\sqrt{\text{N1}}$ amplitudes correlation with			
patient	current	electr.	samples	mean amplitudes	$-\log$ count^{-1}	min str^{-1}	med str^{-1}	wm dist^{-1}
1	3.5 mA	14	32	281±250 µV	0.47 (.007)	**0.50 (.003)**	0.03 (.863)	0.45 (.009)
2	2.5 mA	10	9	208±170 µV	0.45 (.222)	0.57 (.112)	0.01 (.972)	**0.79 (.012)**
3	2.0 mA	14	26	266±248 µV	0.15 (.460)	0.20 (.323)	**0.35 (.082)**	0.01 (.967)
4	5.0 mA	14	27	437±263 µV	0.32 (.098)	**0.54 (.004)**	-0.04 (.845)	0.25 (.205)
5	2.5 mA	14	29	233±157 µV	0.65 (.001)	**0.65 (.001)**	0.46 (.011)	0.38 (.041)
6	2.2 mA	8	7	189±86 µV	-0.25 (.593)	-0.03 (.943)	-0.20 (.669)	**0.32 (.487)**
7	5.0 mA	14	36	292±240 µV	0.62 (.001)	**0.72 (.001)**	0.46 (.005)	0.48 (.003)
8	5.0 mA	14	37	285±199 µV	0.37 (.022)	**0.50 (.002)**	0.01 (.964)	0.44 (.006)
9	5.0 mA	14	44	390±338 µV	0.56 (.001)	**0.62 (.001)**	-0.14 (.363)	0.16 (.298)
				average:	0.37±0.26	**0.47±0.23**	0.11±0.24	0.36±0.21

Table 4: The square roots of N1 amplitudes were strongly positively correlated with the inverse of the shortest streamline lengths (*min str*$^{-1}$) in most of the cases. The three rightmost columns show the Pearson correlation coefficients computed for the quare roots of N1 peak amplitudes paired with the inverse of three studied distance measures. The respective p-values are given in parentheses. The highest scores per patient, spanning between 0.32 and 0.79, are printed in bold. A positive correlation was also held for the inverse of minus log-transformed streamline counts (*−log count*$^{-1}$) in all cases except for Patient 6. Additionally, in order to emphasize the role of uncontrollable factors in experimental setup, the following are specified: current intensity of DES, number of recording electrodes used, number of samples with N1 peaks identified, and average N1 amplitudes with the respective standard deviations.

patient	samples	thresh	max len	JI	sensit	specif	TP	FP	TN	FN
1	32	0.008	25 mm	0.68	0.81	0.94	26 (19%)	6 (4%)	102 (73%)	6 (4%)
2	9	0.014	17 mm	0.46	0.67	0.96	6 (6%)	4 (4%)	87 (87%)	3 (3%)
3	26	0.006	33 mm	0.52	0.85	0.91	22 (11%)	16 (8%)	154 (79%)	4 (2%)
4	27	0.009	36 mm	0.67	0.74	0.97	20 (16%)	3 (2%)	96 (76%)	7 (6%)
5	29	0.007	35 mm	0.54	0.76	0.90	22 (14%)	12 (8%)	113 (73%)	7 (5%)
6	7	0.017	19 mm	0.43	0.86	0.88	6 (9%)	7 (11%)	50 (78%)	1 (2%)
7	36	0.008	26 mm	0.57	0.67	0.94	24 (17%)	6 (4%)	98 (70%)	12 (9%)
8	37	0.008	55 mm	0.61	0.84	0.89	31 (18%)	14 (8%)	117 (70%)	6 (4%)
9	44	0.007	30 mm	0.66	0.89	0.88	39 (23%)	15 (9%)	109 (65%)	5 (3%)
						average:	15±5%	6±3%	75±6%	4±2%

Table 5: Summary of quantitative results of the maximum Jaccard Index (*JI*) classifiers based on the log-transformed streamline counts. The thresholds (*thresh*) on the normalized count-based connectivity measure range between 0.006 (Patient 3) and 0.017 (Patient 6). The column labeled *max len* presents maxima of the shortest lengths among endpoints after applying a threshold. The next three columns show the maximum Jaccard Index together with the sensitivity and specificity of the count-based connectivity classifiers. The last four columns hold the coefficients of the respective confusion matrices (i.e. *TP* – true positives, *FP* – false positives, *TN* – true negatives, *FN* – false negatives). Note that the inter-patient averages gave 6±3% false positives and 4±2% false negatives.

patient	samples	thresh	limit len	JI	sensit	specif	TP	FP	TN	FN
1	32	0.010	18 mm	0.71	0.78	0.97	25 (18%)	3 (2%)	105 (75%)	7 (5%)
2	9	0.020	17 mm	0.39	0.78	0.90	7 (7%)	9 (9%)	82 (82%)	2 (2%)
3	26	0.008	17 mm	0.60	0.81	0.95	21 (11%)	9 (5%)	161 (82%)	5 (2%)
4	27	0.012	19 mm	0.72	0.78	0.98	21 (17%)	2 (2%)	97 (77%)	6 (4%)
5	29	0.009	20 mm	0.51	0.69	0.92	20 (13%)	10 (6%)	115 (75%)	9 (6%)
6	7	0.024	14 mm	0.56	0.71	0.96	5 (8%)	2 (3%)	55 (86%)	2 (3%)
7	36	0.009	21 mm	0.62	0.69	0.96	25 (18%)	4 (3%)	100 (71%)	11 (8%)
8	37	0.009	24 mm	0.74	0.86	0.95	32 (19%)	6 (4%)	125 (74%)	5 (3%)
9	44	0.007	19 mm	0.68	0.89	0.90	39 (23%)	13 (8%)	111 (66%)	5 (3%)
						average:	15±5%	5±2%	76±6%	4±2%

Table 6: Summary of quantitative results of the maximum Jaccard Index (*JI*) classifiers based on the shortest streamline lengths. Here, we simply disregarded all the structural links which were longer than a certain limit length (*limit len*) determined by our threshold (*thresh*) in a length-based connectivity matrix. The thresholds ranged between 0.008 and 0.024, which corresponded to the limit lengths between 14 and 24 mm. The confusion matrix coefficients (i.e. *TP* – true positives, *FP* – false positives, *TN* – true negatives, *FN* – false negatives) were comparable with the ones in the count-based binary connectivity. Although, the inter-patient averages gave a bit lower percent of false positives (5±2%) and minimally higher percent of true negatives (76±6%) than in the other measure.

dependent variable	explanatory variable	macrostructure only		macro- and microstructure		
		R^2 score	RMSE	R^2 score	RMSE	indices included
N1 delay	−log count	0.04±0.55	8±10 ms	0.12±0.31	7±9 ms	{ Tort, MK, RK, ND }
	min str	**0.11±0.27**	**8±9 ms**	**0.33±0.09**	**7±9 ms**	{ Tort, MK, RK, NG, ND }
	med str	-0.23±0.20	9±11 ms	-0.10±0.63	8±10 ms	{ Tort, NG$_\perp$, ODI, AWF }
	wm dist	-0.07±0.17	9±9 ms	-0.09±0.53	8±10 ms	{ Tort, MK, RK, NG$_\perp$, ODI }
N1 amplitude	−log count	**0.06±0.14**	**240±384 µV**	0.10±0.10	237±368 µV	{ FA }
	min str	0.06±0.18	243±370 µV	**0.12±0.19**	**236±356 µV**	{ FA, NG$_\perp$ }
	med str	-0.14±0.17	267±418 µV	0.01±0.10	253±398 µV	{ FA, NG$_\perp$ }
	wm dist	0.01±0.15	256±409 µV	0.06±0.08	246±382 µV	{ FA }

Table 7: Microstructure information improved the accuracy of prediction of the effective connectivity measures, especially N1 delays. For each dependent variable (showed in the first column), i.e. N1 delay and N1 amplitude, a set of four prediction models was built using the respective macrostructural measures as base explanatory variables (second column). The mean R^2 scores and root mean squared errors (RMSE) obtained with the leave-one-patient-out cross-validation are given (with standard deviations) in the columns entitled *macrostructure only*. The same prediction models were extended by adding microstructure indices selected through stepwise linear regression. This modification resulted in a systematic increase of R^2 scores and a decrease of RMSEs, as presented in the columns entitled *macro- and microstructure*. In each case, the best results are printed in bold. The included microstructure indices are provided in the last column. Abbreviations: *Tort* – Tortuosity of the extra-axonal space, *MK* – Mean Kurtosis, *RK* – Radial Kurtosis, *ND* – Non-Gaussianity, *NG$_\perp$* – perpendicular Non-Gaussianity, *ND* – Neurite Density, *ODI* — Orientation Dispersion Index, *AWF* – Axonal Water Fraction, and *FA* – Fractional Anisotropy.